



Spallation of polycarbonate under plate impact loading

Cite as: J. Appl. Phys. **126**, 085105 (2019); <https://doi.org/10.1063/1.5108965>

Submitted: 04 May 2019 . Accepted: 06 August 2019 . Published Online: 23 August 2019

S. J. Ye , H. W. Chai, X. H. Xiao, Y. Cai, X. H. Yao , and S. N. Luo



View Online



Export Citation



CrossMark

Journal of
Applied Physics

SPECIAL TOPIC:
Polymer-Grafted Nanoparticles

Submit Today!

Spallation of polycarbonate under plate impact loading

Cite as: J. Appl. Phys. **126**, 085105 (2019); doi: [10.1063/1.5108965](https://doi.org/10.1063/1.5108965)

Submitted: 4 May 2019 · Accepted: 6 August 2019 ·

Published Online: 23 August 2019



S. J. Ye,^{1,2,3}  H. W. Chai,³ X. H. Xiao,⁴ Y. Cai,^{3,a)} X. H. Yao,^{1,b)}  and S. N. Luo^{2,3}

AFFILIATIONS

¹Department of Engineering Mechanics, South China University of Technology, Guangzhou, Guangdong 510640, People's Republic of China

²Key Laboratory of Advanced Technologies of Materials, Ministry of Education and Institute of Materials Dynamics, Southwest Jiaotong University, Chengdu, Sichuan 610031, People's Republic of China

³The Peac Institute of Multiscale Sciences, Chengdu, Sichuan 610031, People's Republic of China

⁴Advanced Photon Source, Argonne National Laboratory, Argonne, Illinois 60439, USA

^{a)}caiy@pims.ac.cn

^{b)}yaoxh@scut.edu.cn

ABSTRACT

We investigate spallation of polycarbonate under plate impact loading. The Hugoniot equation of state up to ~ 1.3 GPa (corresponding to a peak particle velocity ~ 380 m/s) is obtained, and spall strength and corresponding strain rates are determined at peak shock stresses up to ~ 2.4 GPa (corresponding to a peak particle velocity ~ 600 m/s). With increasing shock strength, the transition from strain-hardening to softening at shock states occurs as a result of shock heating; spall strength remains approximately constant, followed by a rapid drop upon strain softening. Release/tensile melting occurs at higher impact velocities. Three-dimensional void configurations of the postmortem samples are obtained via X-ray computerized tomography. The small voids are flat and curved for low-speed shots but become ellipsoidal for high-speed shots, and their coalescence leads to different shapes likely due to different damage mechanisms.

Published under license by AIP Publishing. <https://doi.org/10.1063/1.5108965>

I. INTRODUCTION

Polycarbonate has a useful balance of temperature resistance, impact resistance, and optical properties and is widely used as an engineering material in transparent elements of dynamic protective equipment. As a thermoplastic polymer, its compression (e.g., equation of state) and tensile properties (e.g., fracture mechanisms) under dynamic extremes are of fundamental interest. The Hugoniot equation of state of polycarbonate was investigated with plate impact and high explosive loading.^{1–5} However, most previous studies focused on shock-state particle velocity above 500 m/s,^{1,3–5} while the peak particle velocity is below 500 m/s (peak stress 1.8 GPa) for many engineering applications.^{6,7}

Upon plate impact loading, shock waves propagate into target and flyer plate and are then reflected at the respective free surfaces as centered simple release (rarefaction) fans traveling in opposite directions. When these two release fans encounter each other, their interaction induces release and an evolving tensile region. Spallation occurs

when the tensile stress exceeds tensile strength.^{8,9} Curran *et al.*^{10,11} employed plate impact to investigate fracture mechanisms in polycarbonate; crack nucleation, growth, and coalescence in recovered samples were analyzed with optical microscopy. Kalthoff and Shockey¹² conducted plate impact experiments on polycarbonate to examine crack instability; a static-fracture-mechanics-based fracture theory was developed for short loading pulses. Besides plate impact loading, spallation of polycarbonate was also investigated with laser shocks. De R  s  guier and Deleignies¹³ performed laser shock experiments on polycarbonate, and a model was constructed via postmortem examination of fracture damage and analyzing the influences of experimental parameters. Despite its engineering importance, quantification of bulk properties such as spall strength and corresponding strain rate has been lacking for polycarbonate, and microscopic characterization of fracture is largely limited to optical microscopy. Three-dimensional (3D) characterization of voids with X-ray computed tomography (CT)^{14,15} is highly desirable for gaining insights into underlying mechanisms of dynamic fracture.

In this work, we investigate the Hugoniot equation of state and spallation in polycarbonate under plate impact loading. The Hugoniot equation of state is obtained up to ~ 1.3 GPa (corresponding to a peak particle velocity of 380 m/s), as a useful complement to previous data. In spallation experiments, free-surface velocity histories are measured up to ~ 1200 m/s, and spall strengths and corresponding strain rates are deduced. Shock-state softening and release/tensile melting are indicated by free-surface velocity histories and lead to rapid changes in spall strength and strain rate, respectively. The postmortem samples are then characterized with CT to obtain 3D void configurations. The shape of small voids differs considerably between low-speed and high-speed shots, and their different growth paths are attributed to different spallation mechanisms (presumably, interchain vs intrachain breakage).

II. EXPERIMENTAL

Commercially available polycarbonate is used for plate impact experiments. At ambient conditions, it has a density of $\rho_0 = 1.20$ g/cm³. Its longitudinal and transverse sound velocities measured with an ultrasonic device are 2.153 km/s and 0.921 km/s, respectively, and the Poisson's ratio is $\nu = 0.388$.

Plate impact experiments are conducted on a single-stage gas gun with a bore diameter of 14 mm. The schematic setups of Hugoniot and spallation experiments are shown in Figs. 1(a) and 1(b), respectively. For both types of experiments, a flyer plate (5) is attached to a polycarbonate sabot (3), with a recess (4) immediately behind it. When a solenoid valve is fired, compressed gas

(He) is released from a high-pressure gas reservoir into gun barrel (1), accelerating the sabot and flyer plate to impact sample (9). The flyer plate velocity (u_{imp}) is measured with an optical beam blocking system (6). For Hugoniot experiments, the front (impact) surface is partially coated with a thin Ag film (10) for reflecting the diagnostic light. A multichannel Doppler pin system (DPS, similar to a photon Doppler velocimeter)^{16,17} is used for measuring shock breakouts at the flyer plate–target interface and the target free surface. Four single-mode optical fibers (11) are set about 0.5 mm away from the target rear (free) surface. Each fiber is connected to a DPS channel.

For spallation experiments, the rear surface of a sample is coated with a thin Ag film. Free-surface velocity (u_{fs}) is measured with a single-channel DPS. Upon impact, the sabot is blocked by sample holder (8), and the shock-loaded sample is stopped by soft materials (14) and “soft-recovered” for CT examination.

Both surfaces of the flyer plate and sample are polished to micrometer level or mirror finish. Flyer plates and samples are both made of polycarbonate for symmetric impact. For Hugoniot experiments, the diameter of both flyer plates and samples is 13.2 mm; the flyer plate thickness is 1.9 mm, and the sample thickness is 2.9 mm or 3.9 mm. To check the effects of lateral release waves on measurements of shock and particle velocities, the optical fiber probes are uniformly distributed at the center and on the circle with a diameter of 4 mm, and the reported velocity measurements are not affected by edge release. For spallation experiments, the diameter and thickness of a flyer plate is 13.2 mm and 0.9 mm, respectively. The sample diameter is set at 9 mm to ensure that both sabot and flyer plate are blocked by the sample holder; the nominal sample thickness is 1.9 mm.

For microstructural characterization,^{18,19} the middle part of a postmortem sample is harvested for CT to investigate crack/void characteristics. CT is a nondestructive three-dimensional (3D) technique capable of resolving internal structure. In this work, CT is conducted at the 2-BM beamline of the Advanced Photon Source with a pixel resolution of $0.87 \mu\text{m}/\text{pixel}$. The photon energy of incident X-rays is 24.9 keV. The X-ray passing through the sample is converted into visible light by a $20 \mu\text{m}$ thick LuAG scintillator and then recorded by a charge coupled device (CCD) camera through a $7.5\times$ lens array. The sample-to-scintillator distance is 60 mm. The CCD array contains 2560×2000 pixels, yielding a field of view of $2.20 \times 1.74 \text{ mm}^2$. One CT scan uniformly collects 1500 projection images within 180° with a 100-ms exposure time for projection. The projections are then reconstructed into a 3D image by a reconstruction program, *TomoPy*.²⁰

III. RESULTS AND DISCUSSION

A. Hugoniot experiments

For symmetric impact, the particle velocity of a shock state (u_p) equals to half of the impact velocity (u_{imp}), i.e., $u_p = \frac{1}{2}u_{\text{imp}}$. Shock velocity (u_s) is determined from the shock transit time (Δt) and sample thickness (h_s) via $u_s = h_s/\Delta t$. Here, Δt is the difference in shock arrival times between the sample front surface and rear surface determined from DPS measurements. The “trigger time” for our DPS system mainly comes from the rise time or response time of the detector, which is about 30 ps and negligible compared

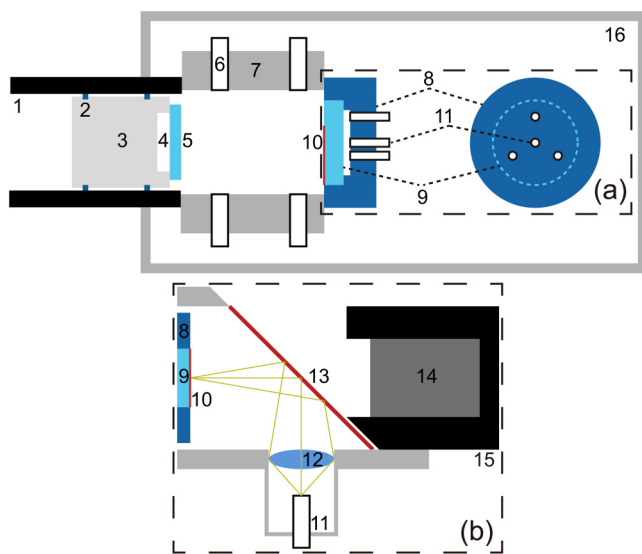


FIG. 1. Schematic setup for plate impact loading: (a) Hugoniot experiments and (b) spallation experiments. 1: gun barrel; 2: O-ring; 3: polycarbonate sabot; 4: recess for release waves; 5: flyer plate; 6: optical fibers and detectors for the optical beam blocking system (OBB); 7: attachment bracket; 8: sample holder; 9: sample; 10: Ag coating; 11: optical fiber connected to the Doppler pin system (DPS); 12: lens; 13: turning mirror; 14: soft materials; 15: recovery bin; 16: vacuum chamber.

TABLE I. Experimental parameters and results of the Hugoniot shots. h_f : flyer plate thickness; h_s : sample thickness; u_{imp} : impact velocity; u_p : shock-state particle velocity; u_s : shock velocity; σ_H : peak stress. Numbers in parentheses denote uncertainties in the last one or two significant digits.

Shot number	h_f (mm)	h_s (mm)	u_{imp} (km/s)	u_p (km/s)	u_s (km/s)	σ_H (GPa)
MP322	1.931 (2)	2.910 (2)	0.168 (1)	0.084 (1)	2.457 (15)	0.248 (2)
MP330	1.923 (2)	2.931 (2)	0.192 (1)	0.096 (1)	2.478 (3)	0.285 (2)
MP337	1.919 (2)	2.929 (2)	0.226 (1)	0.113 (1)	2.472 (3)	0.335 (2)
MP296	1.922 (2)	3.930 (2)	0.231 (1)	0.116 (1)	2.502 (23)	0.347 (4)
MP301	1.927 (2)	3.941 (2)	0.265 (1)	0.133 (1)	2.501 (6)	0.398 (3)
MP343	1.933 (2)	2.931 (2)	0.303 (2)	0.152 (1)	2.519 (9)	0.458 (3)
MP349	1.922 (2)	2.928 (2)	0.310 (2)	0.155 (1)	2.529 (3)	0.470 (3)
MP355	1.928 (2)	2.937 (2)	0.337 (2)	0.169 (1)	2.560 (25)	0.518 (6)
MP362	1.917 (2)	2.930 (2)	0.345 (2)	0.173 (1)	2.553 (5)	0.528 (4)
MP314	1.924 (2)	3.933 (2)	0.385 (2)	0.193 (1)	2.566 (21)	0.593 (6)
MP318	1.920 (2)	3.945 (2)	0.441 (2)	0.221 (1)	2.599 (3)	0.688 (5)
MP367	1.931 (2)	2.930 (2)	0.547 (3)	0.274 (1)	2.685 (7)	0.881 (6)
MP371	1.929 (2)	2.940 (2)	0.689 (3)	0.345 (2)	2.775 (2)	1.147 (8)
MP380	1.921 (2)	2.932 (2)	0.758 (4)	0.379 (2)	2.828 (4)	1.290 (9)

to shock rise the duration of interest (1–2 μs). The peak shock stress is then obtained as $\sigma_H = \rho_0 u_s u_p$. In our experiments, four DPS channels are used for averaging.

A total of 14 Hugoniot shots are fired, and the experimental parameters and results are summarized in Table I. The u_s – u_p data from this work and the literature^{1–5,13} are presented in Fig. 2. Previous experiments largely explored the pressure range above 1 GPa; our data are in the range of $\sigma_H = 0.248$ –1.290 GPa and agree with the literature data. The u_s – u_p data can be described with a quadratic relation (Fig. 2, inset). The fitting yields $u_s = 2.39 + 0.70u_p + 1.24u_p^2$.

B. Spallation experiments

A total of 15 spallation shots are fired, and the free-surface velocity histories are shown in Fig. 3. We use the free-surface velocity history labeled with A–F in Fig. 3 to illustrate three processes:

dynamic compression, subsequent release, and spallation. Segment AB indicates the arrival of shock wave at the rear surface and then reach a Hugoniot/shock state (BC). The arrival of the release fan from the back surface of the flyer plate leads to a velocity drop (CD). The interaction of this release fan with that initiated from the sample free surface gives rise to release and tension in the sample interior, and spallation is resulted when the tensile stress exceeds the spall strength at a specific loading condition. The ensuing velocity increase (DE and EF) is induced by the arrival of a compression wave originated from the spall plane within the sample. The reacceleration beginning at E is a typical signature of spall. DE is attributed to independent growth of isolated cracks or voids, and EF, to their coalescence.^{21,22} The slope of EF reflects the

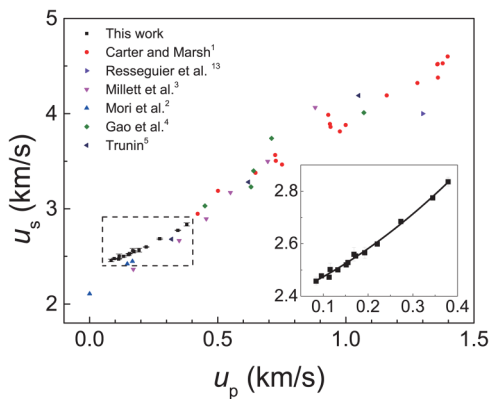


FIG. 2. The u_s – u_p plot of polycarbonate. Data are from this work and the literature.^{1–5,13} Inset: an enlarged view of the region delimited with the dashed rectangle; the solid line denotes quadratic fitting to the data of this work.

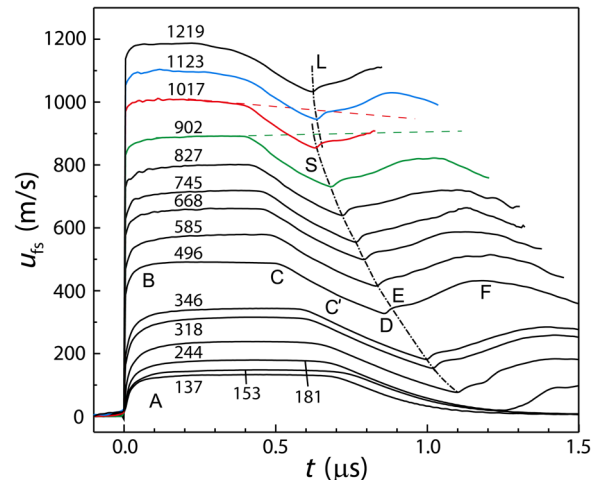


FIG. 3. Free-surface velocity histories for spallation experiments. Numbers refer to impact velocities in m/s. L: liquid; S: solid.

fracture rate during spallation.²³ The compressive yield strength of polycarbonate is very low, so the elastic shock speed is close to the initial longitudinal sound velocity (2.153 km/s). Even for a low-speed shot ($u_{\text{imp}} = 168$ m/s), the plastic shock speed (2.457 km/s) is higher than the elastic shock speed, i.e., the elastic precursor is overtaken by the plastic shock, so HEL is not detected in our experiments.

Free-surface velocity histories allow us to deduce such quantities as spall strength and tensile strain rate. Spall strength is calculated from the pullback velocity with the acoustic method^{24–27}

$$\sigma_{\text{sp}} \approx \rho_0 C_L \Delta u \frac{1}{1 + \frac{C_L}{C_B}}, \quad (1)$$

where C_L is longitudinal sound velocity, C_B is bulk sound velocity, and the pullback velocity of $\Delta u = u_{\text{fs,D}} - u_{\text{fs,C}}$. Tensile strain rate near spallation (e.g., C'D in Fig. 3) can be estimated with^{28,29}

$$\dot{\epsilon} \approx \frac{1}{2C_B} \left. \frac{du_{\text{fs}}(t)}{dt} \right|_{\text{release}}. \quad (2)$$

The average value of $\dot{\epsilon}$ near the pullback is used in our discussion.

As shown in Fig. 3, free-surface velocity histories show a clear pullback (spallation) for $u_{\text{imp}} > 153$ m/s. Although no pullback is observed for $u_{\text{imp}} = 153$ and 137 m/s, CT examination reveals minor damage (see below) which does not yield sufficiently strong signature on a free-surface velocity history.

With increasing impact velocity, longitudinal sound velocity (for the release fan originated from the flyer plate free surface) increases, so spall pullback shifts toward the left on a $u_{\text{fs}}(t)$ curve. For $u_{\text{imp}} \leq 1017$ m/s, the trajectory of the pullback follows the same trend (the dot-dashed line “L” in Fig. 3). When impact

velocity increases from 1017 m/s to 1123 m/s, the pullback begins to shift toward the right. The reversal is attributed to release/tensile melting (transition 2 or T2) which induces a sudden drop in sound velocity. On the other hand, the shock plateaus of the free-surface velocity curves in Fig. 3 show different features at different impact velocity regimes. u_{fs} increases slightly with time on the plateau for $u_p \leq 902$ m/s (the green dashed line in Fig. 3), but begins to decrease for $u_p \geq 1017$ m/s (the red dashed line), indicating a softening transition at shock states (T1). This strain-hardening to strain-softening transition is induced by the combination of shock compression and shock-induced heating and may affect the following release and tensile processes.

Impact velocity, peak stress, spall strength, and tensile strain rate together with experimental parameters are summarized in Table II. Spall strength and tensile strain rate are also plotted as functions of σ_H in Fig. 4. Spall strength remains nearly unchanged under $\sigma_H \leq 1.601$ GPa, followed by a sudden drop at $\sigma_H = 1.872$ GPa and a continuous decrease at higher peak stresses. The sudden drop in σ_{sp} [T1 in Fig. 4(a)] is consistent with the softening transition in Fig. 3. The continuous decrease is due to shock heating of the sample.

On the basis of gas gun loading experiments on polycarbonate, Curran *et al.*¹⁰ and Majewski *et al.*³⁰ obtained spall strengths of 0.167 GPa and 0.161 GPa, respectively, slightly lower than our result (~ 0.19 GPa). In a laser shock study, De R  s  guier and Deleignies¹³ reported a spall strength of 1.3 GPa in the absence of particle velocity measurements; a possible cause is the higher strain rates in laser experiments.

Tensile strain rate increases with increasing peak stress for most shots; however, a sudden decrease occurs at $\sigma_H = 2.139$ GPa [T2 in Fig. 4(b)], and then $\dot{\epsilon}$ increases again. Normally, strain rate increases with increasing peak stress. The drop in strain rate is due to release/tensile melting (T2) prior to spall, consistent with the pullback feature discussed above. Since the sound velocity of liquid

TABLE II. Experimental parameters and results for the spallation shots. h_f : flyer plate thickness; h_s : sample thickness; u_{imp} : impact velocity; σ_H : peak stress; σ_{sp} : spall strength; $\dot{\epsilon}$: tensile strain rate; Φ : average sphericity for each shot. Numbers in parentheses denote uncertainties in the last one, two, or three significant digits.

Shot number	h_f (mm)	h_s (mm)	u_{imp} (km/s)	σ_H (GPa)	σ_{sp} (GPa)	$\dot{\epsilon}$ (10^5 s^{-1})	Φ
MP427	0.917 (2)	1.907 (2)	0.137 (1)	0.201 (3)	0.057
MP428	0.942 (2)	1.912 (2)	0.153 (1)	0.225 (3)	0.026
MP435	0.908 (2)	1.905 (2)	0.181 (1)	0.268 (3)	0.192 (5)	0.446 (14)	...
MP441	0.922 (2)	1.911 (2)	0.244 (1)	0.365 (3)	0.193 (5)	0.749 (29)	0.071
MP449	0.920 (2)	1.905 (2)	0.318 (2)	0.484 (4)	0.195 (5)	0.858 (50)	0.133
MP456	0.927 (2)	1.916 (2)	0.346 (2)	0.529 (4)	0.195 (5)	0.883 (38)	0.198
MP459	0.910 (2)	1.927 (2)	0.496 (2)	0.786 (5)	0.196 (5)	1.018 (48)	...
MP462	0.920 (2)	1.917 (2)	0.585 (3)	0.949 (5)	0.197 (5)	1.030 (48)	...
MP467	0.917 (2)	1.917 (2)	0.668 (3)	1.108 (6)	0.195 (5)	1.002 (52)	...
MP468	0.932 (2)	1.913 (2)	0.745 (4)	1.262 (6)	0.197 (5)	1.062 (81)	...
MP470	0.922 (2)	1.903 (2)	0.827 (4)	1.435 (7)	0.193 (5)	1.078 (81)	...
MP475	0.907 (2)	1.893 (2)	0.902 (5)	1.601 (8)	0.193 (5)	1.165 (87)	...
MP476	0.904 (2)	1.892 (2)	1.017 (5)	1.872 (9)	0.165 (4)	1.236 (101)	...
MP478	0.905 (2)	1.892 (2)	1.123 (6)	2.139 (10)	0.160 (4)	1.011 (90)	...
MP480	0.905 (2)	1.892 (2)	1.219 (6)	2.398 (11)	0.157 (4)	1.297 (106)	...

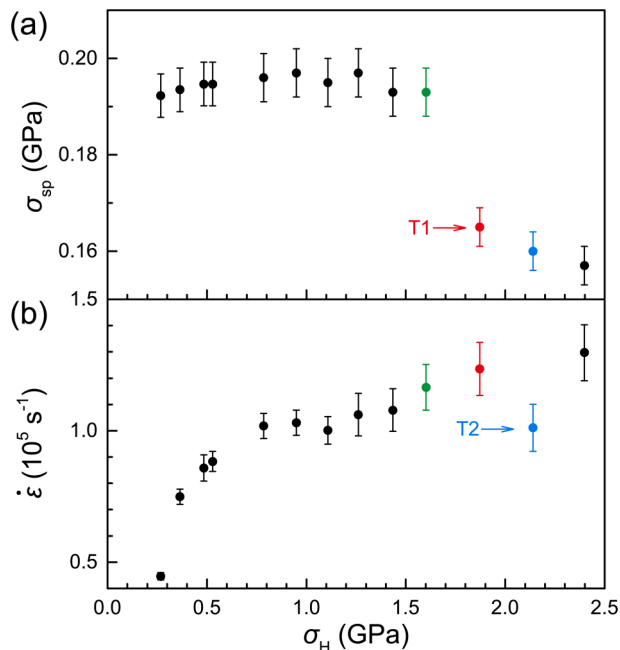


FIG. 4. (a) Spall strength and (b) tensile strain rate as functions of peak shock stress. T1 and T2 denote the first and second transitions.

is smaller than solid, the corresponding release path is temporally stretched, resulting in a smaller $\dot{\epsilon}$. At higher peak stresses ($\sigma_H = 2.398$ GPa), sound speed of the melt also increases, so $\dot{\epsilon}$ increases again.

We compare the tensile strength of polycarbonate under different strain rates as measured with materials testing system (MTS), split Hopkinson tension bar (SHTB), and gas gun loading in Fig. 5. As expected, tensile strength increases with increasing strain rate. The strain rate sensitivity is relatively weak in MTS and SHTB experiments: the tensile strength increases only 50% across 6 orders of magnitude of strain rate. However, it increases by $\sim 100\%$ from SHTB to gas gun loading with only an increase of two orders. This sudden increase may be caused by the transition from ductile failure to brittle failure.

The apparent insensitivity of σ_{sp} to strain rate and peak stress prior to T1 [Fig. 4(a)] appears to be against classical strength theory. A main reason is that the thermoplastic nature of polycarbonate renders it weaker against shock-induced heating.²⁷ While strain rate increases with increasing peak stress, the strain-rate-strengthening effect on spall strength is offset by the weakening effect of shock heating, and consequently, σ_{sp} remains approximately a constant prior to T1.

C. Void characterization

Microscopic features of spall damage in postmortem polycarbonate samples are examined with CT. To minimize the effects of edge release on damage analysis, only the middle part of a

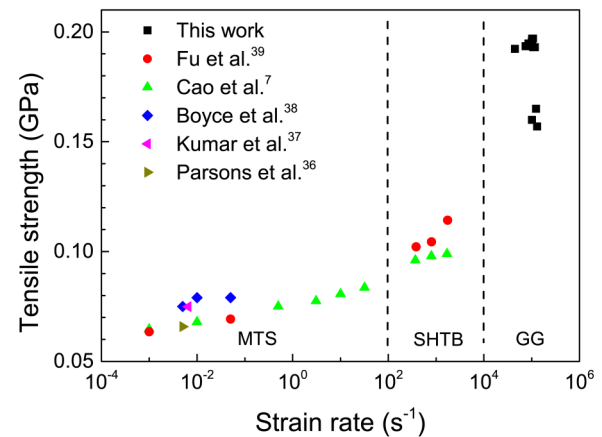


FIG. 5. Tensile strength of polycarbonate under different loadings as a function of strain rate. Data are from this work and the literature.^{7,31–34} MTS: materials testing system; SHTB: split Hopkinson tension bar; GG: gas gun.

recovered specimen is used for CT characterization. Note that shock recovery inevitably involves complicated wave interactions after spallation, so postmortem void characterization may deviate from the actual characteristics. The dimensions of a CT sample are $1.2 \times 0.6 \times 3.2$ mm³ [Fig. 6(a)]. CT characterization is conducted for five incipient and full spallation shots, and 3D configurations of voids are shown in Figs. 6(b)–6(d). For high-speed shots with $u_{imp} > 400$ m/s, the shocked samples break into pieces so CT characterization is not conducted.

1. Void growth and coalescence

The shape of small voids differs considerably between a low-speed [137 m/s, Fig. 6(b)] and a high-speed shot [318 m/s, Fig. 6(c)]: thin and curved for the former shot and ellipsoidal for the latter shot. The ellipsoidlike voids are quite common for a variety of materials.^{18,22,35,36} Similar to other polymers, polycarbonate is held together by weaker van der Waals forces between molecular chains, and stronger covalent bonds between intramolecular atoms. For low-speed shots, local tensile stress is sufficient to overcome the van der Waals force and create elongated gaps between molecular chains. However, further damage is hindered by the covalent bonds at early stages, resulting in elongated curved cracks between separated molecular chains. In contrast, high tensile stress breaks the covalent bonds at early stages for high-speed shots, resulting in ellipsoidlike voids.

For low-speed shots, small voids grow mainly in the xz -plane. The stress fields of two close voids interact with each other during growth,¹⁰ and the two voids grow toward each other and finally merge. Coalescence of voids and small cracks leads to elongated curved cracks. As two cracks on different xz -planes coalesce, their stress fields attract, and oblique cracks [Fig. 6(d)] form as the result of the evolution of stress fields. Unlike ductile failure under low strain rates, these cracks indicate that polycarbonate undergoes

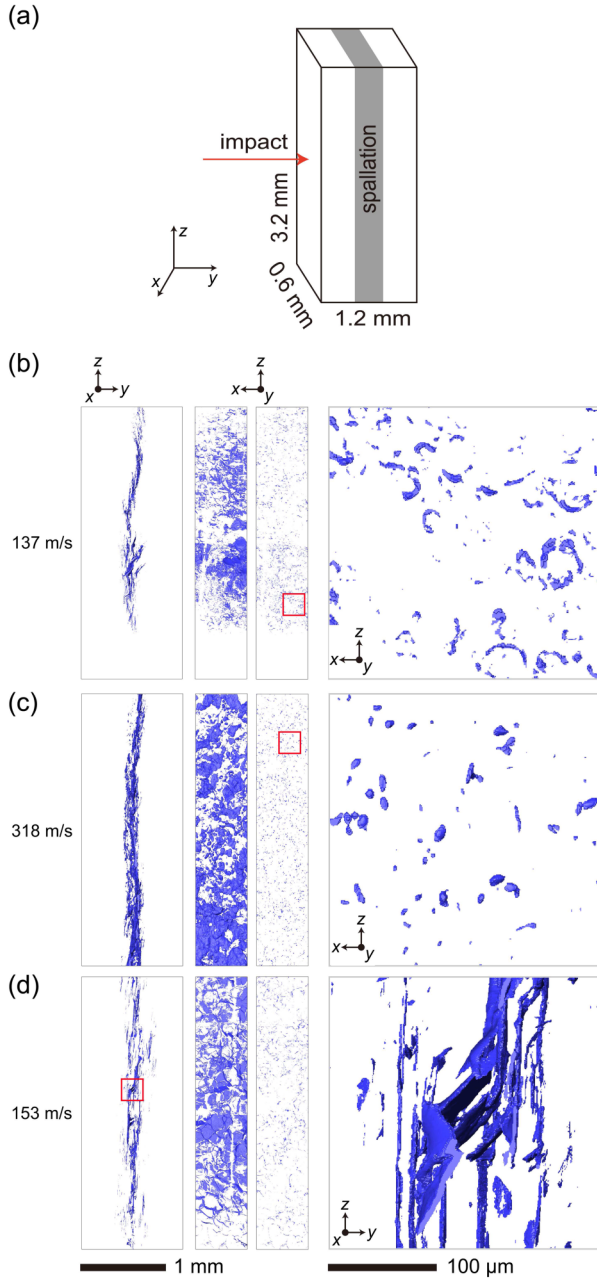


FIG. 6. (a) Geometry of a CT sample. Impact is along the y -axis. (b)–(d) 3D void/crack configurations at different impact velocities as noted. The third column shows only the voids smaller than $659 \mu\text{m}^3$. The forth column corresponds to the regions denoted with red rectangles.

brittle failure under high strain rate loading as in many other materials.^{37,38}

For high-speed shots [Fig. 6(c)], voids grow not only on the xz -plane (parallel to the spall plane) but also along the impact

direction (perpendicular to the spall plane, the y -axis). Thus, the damage zone along the impact direction is wider. Oblique cracks are less common than in the lower-speed cases, due to the widening of cracks and the narrowing of the whole spallation region along the impact direction.

2. Void morphology and size distribution

The topology of a specific void can be characterized with gyration tensor \mathbf{G} ,^{35,39}

$$G_{\alpha\beta} = \frac{1}{V} \sum_{i=1}^M (r_{\alpha i} - r_{\alpha})(r_{\beta i} - r_{\beta}), \quad (3)$$

where $G_{\alpha\beta}$ is the $\alpha\beta$ component of gyration tensor \mathbf{G} ($\alpha, \beta = x, y, z$); V is the volume of the void consisting of M voxels; $r_{\alpha i}$ and $r_{\beta i}$ are α and β coordinates of voxel i , respectively; and r_{α} and r_{β} are α and β coordinates of the barycenter of the void, respectively.

We then calculate three eigenvalues R_j ($j = 1, 2, 3$) of the gyration tensor and construct an ellipsoid with three semiaxes, $\sqrt{5R_j}$. Sphericity (Φ) is then obtained by dividing the shortest semiaxis by the longest semiaxis and used to quantify the shape feature of a void. Φ varies between 0 and 1; $\Phi = 1$ for a sphere and $\Phi = 0$ if the ellipsoid flattens into an ellipse.

To characterize the distribution of sphericity, we calculate relative fraction of sphericity (f_r) via binning sphericity values of voids with

$$f_r(i) = \frac{N_{\Phi \in [l, r]}}{N_{\Phi \in (0, 1]}}. \quad (4)$$

Here, N is the number of voids, $l = 0.05(i - 1)$, $r = 0.05i$, i is the serial number of a bin and the binning width is $\Delta\Phi = 0.05$. Figure 7(a) shows $f_r(\Phi)$ for different impact velocities.

For voids with a given volume, their average sphericity ($\bar{\Phi}$) is also calculated with nonlinear binning as

$$\bar{\Phi}(i) = \frac{\sum_{V_j \in [a, b]} \Phi_j}{N_{V_j \in [a, b]}}, \quad (5)$$

where i is the serial number of a bin and V_j and Φ_j are the volume and sphericity of j th void. a and b are chosen to start at the smallest distinguishable voids and generate a proper interval for plotting: $a = 10^{-0.108+0.528i} \mu\text{m}^3$ and $b = 10^{-0.108+0.528(i+1)} \mu\text{m}^3$.^{36,40} The volume of the i th bin is located in $[a, b)$. Figure 7(b) shows the $\bar{\Phi}(V)$ curves for representative shots.

When calculating the three semiaxes for the weakest spall shot (137 m/s), the longest one is underestimated due to the curved shape of voids or cracks. Since the sphericity is inversely proportional to the longest semiaxis, sphericity is overestimated for this shot [Fig. 7(a)]. Similar to the case of dual-phase Ti-6Al-4V,¹⁹ the relative fraction of sphericity decreases sharply with increasing sphericity. With increasing impact velocities, f_r of small sphericity decreases but f_r of large sphericity increases, except for shot MP427 ($u_{\text{imp}} = 137 \text{ m/s}$). For low-speed shots, tensile strain rates are relatively low to permit longer nucleation time, resulting in larger

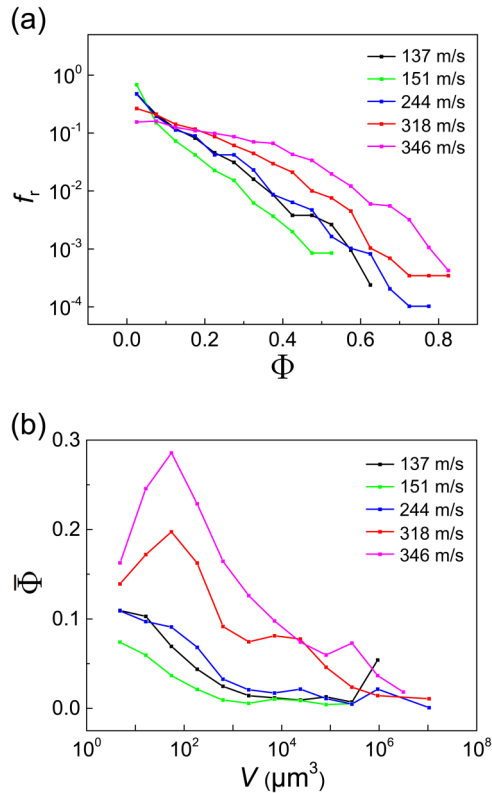


FIG. 7. (a) Relative fraction of voids vs sphericity, $f_r(\Phi)$, for different impact velocities. (b) Average sphericity vs void volume, $\bar{\Phi}(V)$, for different impact velocities.

f_r of small sphericity. Under higher tensile strain rates as in high-speed shots, void coalescence is more rapid and pronounced, giving rise to higher sphericity.

Average sphericity is obtained as a function of void volume [Fig. 7(b)]. The relatively small number of large cracks leads to larger errors. All the average sphericity are less than 0.3, indicating that most voids are flat (“penny” shaped). The average sphericity increases with increasing impact velocity except for the weakest spall shot (Table II).⁴¹ As mentioned in Sec. III B, shock-induced heating increases with increasing impact velocity. The temperature rise reduces deviatoric stress during spallation, leading to a more hydrostatic tensile state for void nucleation and growth, resulting in higher void sphericity for high-speed shots [Fig. 7(b)]. For low-speed shots, the average sphericity decreases with increasing void volume,⁴¹ as a result of preferred, anisotropic, growth and coalescence of voids and cracks.⁴² For high-speed shots, sphericity first increases and then decreases with increasing volume. Voids are initially of irregular shapes in high-speed shots; however, they become ellipsoid during subsequent growth, resulting in increase of sphericity. After that, the voids coalesce randomly, leading to the irregular shapes and thus the decrease sphericity of large voids.⁴²

The number density (d_n) of voids as a function of void volume is calculated via binning with the same bin width as for average sphericity,

$$d_n(i) = \frac{N_{V_j \in [a,b]}}{b-a}. \quad (6)$$

Here, i refers to the i th volume bin, V_j is the volume of the j th void, and a and b are the same as Eq. (5).

d_n of two representative shots MP427 and MP449 are shown in Fig. 8(a). The trend of d_n is similar to the work of Curran *et al.*¹⁰ d_n of small voids decreases and large voids increases with increasing impact velocity for these two shots. This indicates different mechanisms in void growth. As mentioned above, local tensile stress only overcomes the Van der Waals forces and covalent bonds are retained during the tensile process. In this situation, tensile stress is kept for a relatively long time to produce more small nuclei of voids. However, the intense tensile wave in high-speed shots quickly breaks the covalent bonds inside molecular chains. The tensile stress is only sustained for a short time and thus

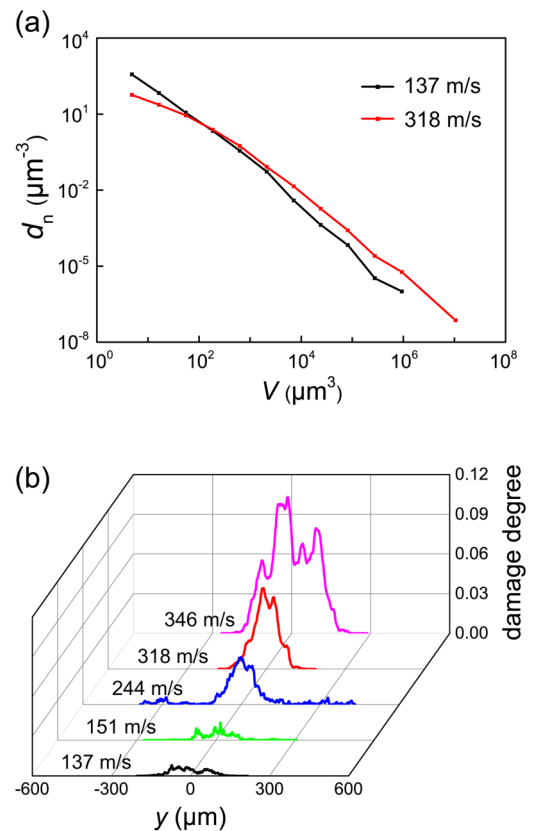


FIG. 8. (a) Size distribution of voids for different impact velocities: void number density vs void volume, $d_n(V)$. (b) Profiles of damage degree along the y -axis (impact direction) for different impact velocities. $y = 0$ is set at the center of a spallation zone.

only a small number of nuclei is generated. Thus, stronger loading creates more severe damage, resulting in more large voids for high-speed shots.

Damage degree is defined as the ratio of damaged volume to the whole volume under consideration. The profiles of damage degree along the impact direction (perpendicular to the spall plane) for different impact velocities are presented in Fig. 8(b). The distribution of damage degree is similar to the fitting results of Curran *et al.*¹⁰ Damage degree increases with increasing impact velocity. The damage region widens with increasing impact velocity for low-speed and high-speed shots, respectively. This is because the damage region becomes wider with increasing peak stress under the same damage mechanism. However, the spallation region narrows abruptly between shot MP441 (244 m/s) and MP449 (318 m/s). The reason here is the same as the transition in number density of these two shots. The break of covalent bonds accelerate the release of stress, resulting in a narrower spallation region.

IV. CONCLUSIONS

The Hugoniot equation of state of polycarbonate is obtained up to ~ 1.3 GPa (corresponding to a peak particle velocity of 380 m/s), as a useful complement to previous data. Spallation experiments yield free-surface velocity histories up to ~ 1200 m/s, and spall strength and corresponding strain rates are deduced. 3D void configurations of the postmortem samples are obtained via CT.

With increasing shock strength, there is a transition from strain-hardening to strain-softening at the peak states as a result of shock-induced heating; spall strength remains approximately a constant (~ 0.195 GPa) as a combined result of shock-induced heating and strain-rate strengthening and undergoes a sharp drop upon the strain-softening at a peak stress of 1.6–1.9 GPa. The small voids are flat and curved for low-speed shots but become ellipsoidal for high-speed shots, and their coalescence leads to different shapes likely due to different damage mechanisms (interchain vs intra-chain breakage).

ACKNOWLEDGMENTS

This work was supported by the National Natural Science Foundation of China (NNSFC, Grant No. 11627901). Use of the Advanced Photon Source, an Office of Science User Facility operated for the U.S. Department of Energy (DOE) Office of Science by Argonne National Laboratory, was supported by the U.S. DOE under Contract No. DE-AC02-06CH11357.

REFERENCES

- ¹W. J. Carter and S. P. Marsh, Hugoniot equation of state of polymers, Technical report, Los Alamos National Lab, NM, USA, 1995.
- ²Y. Mori and K. Nagayama, "Shock Hugoniot curves for several polymeric materials in 0.5-GPa shock stress," in *23rd International Congress on High-Speed Photography and Photonics* (International Society for Optics and Photonics, 1999), Vol. 3516, pp. 241–246.
- ³J. C. F. Millett and N. K. Bourne, "Shock and release of polycarbonate under one-dimensional strain," *J. Mater. Sci.* **41**(6), 1683–1690 (2006).
- ⁴Y. B. Gao, W. Zhang, G. Wei, Y. G. Ni, W. Huang, X. M. Cai, and N. Ye, "A new approach for Hugoniot equation of state of polycarbonate," *Measurement* **68**, 246–256 (2015).

- ⁵R. F. Trunin, "Shock compression of condensed materials (laboratory studies)," *Phys. Uspekhi* **44**(4), 371–396 (2001).
- ⁶P. Yu, X. Yao, Q. Han, S. Zang, and Y. Gu, "A visco-elastoplastic constitutive model for large deformation response of polycarbonate over a wide range of strain rates and temperatures," *Polymer* **55**(25), 6577–6593 (2014).
- ⁷K. Cao, X. Z. Ma, B. S. Zhang, Y. Wang, and Y. Wang, "Tensile behavior of polycarbonate over a wide range of strain rates," *Mater. Sci. Eng. A* **527**(16–17), 4056–4061 (2010).
- ⁸M. M. Shahzamanian, "Implementation of a rate dependent tensile failure model for brittle materials in Abaqus," *Int. J. Impact Eng.* **97**, 127–147 (2016).
- ⁹A. M. Rajendran and J. L. Kroupa, "Impact damage model for ceramic materials," *J. Appl. Phys.* **66**(8), 3560–3565 (1989).
- ¹⁰D. R. Curran, D. A. Shockey, and L. Seaman, "Dynamic fracture criteria for a polycarbonate," *J. Appl. Phys.* **44**(9), 4025–4038 (1973).
- ¹¹D. R. Curran, L. Seaman, and D. A. Shockey, "Dynamic failure of solids," *Phys. Rep.* **147**(5–6), 253–388 (1987).
- ¹²J. F. Kalthoff and D. A. Shockey, "Instability of cracks under impulse loads," *J. Appl. Phys.* **48**(3), 986–993 (1977).
- ¹³T. De Ressaiguier and M. Deleignies, "Spallation of polycarbonate under laser-driven shocks," *Shock Waves* **7**(6), 319–324 (1997).
- ¹⁴M. Dierolf, A. Menzel, P. Thibault, P. Schneider, C. M. Kewish, R. Wepf, O. Bunk, and F. Pfeiffer, "Ptychographic x-ray computed tomography at the nanoscale," *Nature* **467**(7314), 436 (2010).
- ¹⁵A. Thompson, I. Maskery, and R. K. Leach, "X-ray computed tomography for additive manufacturing: A review," *Meas. Sci. Technol.* **27**(7), 072001 (2016).
- ¹⁶O. T. Strand, D. R. Goosman, C. Martinez, T. L. Whitworth, and W. W. Kuhlow, "Compact system for high-speed velocimetry using heterodyne techniques," *Rev. Sci. Instrum.* **77**(8), 083108 (2006).
- ¹⁷C. Q. Jiang, Y. Li, Q. C. Liu, X. M. Zhou, and S. N. Luo, "A 532 nm fiber-optic displacement interferometer for low-velocity impact experiments," *Rev. Sci. Instrum.* **89**(2), 023101 (2018).
- ¹⁸Y. Yao, H. W. Chai, C. Li, B. X. Bie, X. H. Xiao, J. Y. Huang, M. L. Qi, and S. N. Luo, "Deformation and damage of sintered low-porosity aluminum under planar impact: Microstructures and mechanisms," *J. Mater. Sci.* **53**(6), 4582–4597 (2018).
- ¹⁹J. Tan, L. Lu, H. Y. Li, X. H. Xiao, Z. Li, and S. N. Luo, "Anisotropic deformation and damage of dual-phase Ti-6Al-4V under high strain rate loading," *Mater. Sci. Eng. A* **742**, 532–539 (2019).
- ²⁰D. Gürsoy, F. D. Carlo, X. H. Xiao, and C. Jacobsen, "Tomopy: A framework for the analysis of synchrotron tomographic data," *J. Synchrotron Radiat.* **21**(Pt 5), 1188–1193 (2014).
- ²¹A. K. Zurek, W. R. Thissell, J. N. Johnson, D. L. Tonks, and R. Hixson, "Micromechanics of spall and damage in tantalum," *J. Mater. Process. Technol.* **60**(1–4), 261–267 (1996).
- ²²C. Li, B. Li, J. Y. Huang, H. H. Ma, M. H. Zhu, J. Zhu, and S. N. Luo, "Spall damage of a mild carbon steel: Effects of peak stress, strain rate and pulse duration," *Mater. Sci. Eng. A* **660**, 139–147 (2016).
- ²³G. I. Kanel and A. V. Utkin, "Estimation of the spall fracture kinetics from the free-surface velocity profiles," *AIP Conf. Proc.* **370**, 487–490 (1996).
- ²⁴T. Antoun, D. R. Curran, L. Seaman, G. I. Kanel, S. V. Razorenov, and A. V. Utkin, *Spall Fracture* (Springer Science & Business Media, 2003).
- ²⁵G. I. Kanel, "Spall fracture: Methodological aspects, mechanisms and governing factors," *Int. J. Fract.* **163**(1–2), 173–191 (2010).
- ²⁶G. V. Stepanov, "Spall fracture of metals by elastic-plastic loading waves," *Probl. Prochn.* **8**, 66–70 (1976).
- ²⁷Y. Cai, H. A. Wu, and S. N. Luo, "Spall strength of liquid copper and accuracy of the acoustic method," *J. Appl. Phys.* **121**(10), 105901 (2017).
- ²⁸B. Arman, S. N. Luo, T. C. Germann, and T. Çağın, "Dynamic response of Cu₆Zr₅4 metallic glass to high-strain-rate shock loading: Plasticity, spall, and atomic-level structures," *Phys. Rev. B* **81**(14), 144201 (2010).
- ²⁹S. N. Luo, Q. An, T. C. Germann, and L. B. Han, "Shock-induced spall in solid and liquid Cu at extreme strain rates," *J. Appl. Phys.* **106**(1), 013502 (2009).

- ³⁰P. Majewski, Y. M. Gupta, and L. Seaman, "Tension-recompression response of shock loaded polycarbonate α ," in *Shock Waves in Condensed Matter* (Springer, 1986), pp. 407–411.
- ³¹E. Parsons, M. C. Boyce, and D. M. Parks, "An experimental investigation of the large-strain tensile behavior of neat and rubber-toughened polycarbonate," *Polymer* **45**(8), 2665–2684 (2004).
- ³²V. Kumar, M. VanderWel, J. Weller, and K. Seeler, "Experimental characterization of the tensile behavior of microcellular polycarbonate foams," *J. Eng. Mater. Technol.* **116**(4), 439–445 (1994).
- ³³M. C. Boyce and E. M. Arruda, "An experimental and analytical investigation of the large strain compressive and tensile response of glassy polymers," *Polym. Eng. Sci.* **30**(20), 1288–1298 (1990).
- ³⁴S. Q. Fu, Y. Wang, and Y. Wang, "Tension testing of polycarbonate at high strain rates," *Polym. Test.* **28**(7), 724–729 (2009).
- ³⁵L. Soulard, J. Bontaz-Carion, and J. P. Cuq-Lelandais, "Experimental and numerical study of the tantalum single crystal spallation," *Eur. Phys. J. B* **85**(10), 332 (2012).
- ³⁶J. Bontaz-Carion and Y. P. Pellegrini, "X-ray microtomography analysis of dynamic damage in tantalum," *Adv. Eng. Mater.* **8**(6), 480–486 (2006).
- ³⁷N. J. Petch, "The ductile-brittle transition in the fracture of α -iron: I," *Philos. Mag.* **3**(34), 1089–1097 (1958).
- ³⁸B. Tanguy, J. Besson, R. Piques, and A. Pineau, "Ductile to brittle transition of an a508 steel characterized by Charpy impact test: Part I: Experimental results," *Eng. Fract. Mech.* **72**(1), 49–72 (2005).
- ³⁹D. N. Theodorou and U. W. Suter, "Shape of unperturbed linear polymers: Polypropylene," *Macromolecules* **18**(6), 1206–1214 (1985).
- ⁴⁰S. Chen, H. W. Chai, A. M. He, T. Tschentscher, Y. Cai, and S. N. Luo, "Resolving dynamic fragmentation of liquids at the nanoscale with ultrafast small-angle x-ray scattering," *J. Synchrotron Radiat.* **26** (2019).
- ⁴¹A. D. Brown, Q. Pham, E. V. Fortin, P. Peralta, P. Patterson, J. P. Escobedo, E. K. Cerreta, S. N. Luo, D. Dennis-Koller, D. Byler *et al.*, "Correlations among void shape distributions, dynamic damage mode, and loading kinetics," *Miner. Metals Mater. Soc.* **69**(2), 198–206 (2017).
- ⁴²Y. Yang, J. Chen, Z. Peng, Z. Guo, T. Tang, H. Hu, and Y. Hu, "X-ray quantitative analysis on spallation response in high purity copper under sweeping detonation," *Mater. Sci. Eng. A* **667**, 54–60 (2016).